Monthly Notices
of the
ROYAL ASTRONOMICAL SOCIETY

MNRAS **458,** 2323–2335 (2016)
Advance Access publication 2016 March 1

doi:10.1093/mnras/stw471

Line-driven ablation of circumstellar discs – I. Optically thin decretion discs of classical Oe/Be stars

Nathaniel Dylan Kee,[1]★ Stanley Owocki[1] and J. O. Sundqvist[2,3]

[1] *Department of Physics and Astronomy, Bartol Research Institute, University of Delaware, Newark, DE 19716, USA*
[2] *Centro de Astrobiologia, Instituto Nacional de Tecnica Aerospacial, E-28850 Torrejon de Ardoz, Madrid, Spain*
[3] *Instituut voor Sterrenkunde, KU Leuven, Celestijnenlaan 200D, B-3001 Leuven, Belgium*

Accepted 2016 February 25. Received 2016 February 25; in original form 2015 December 10

ABSTRACT

The extreme luminosities of massive, hot OB stars drive strong stellar winds through line-scattering of the star's UV continuum radiation. For OB stars with an orbiting circumstellar disc, we explore here the effect of such line-scattering in driving an *ablation* of material from the disc's surface layers, with initial focus on the marginally *optically thin decretion* discs of classical Oe and Be stars. For this we apply a multidimensional radiation-hydrodynamics code that assumes simple optically thin ray tracing for the stellar continuum, but uses a multiray Sobolev treatment of the line transfer; this fully accounts for the efficient driving by non-radial rays, due to desaturation of line-absorption by velocity gradients associated with the Keplerian shear in the disc. Results show a dense, intermediate-speed surface ablation, consistent with the strong, blueshifted absorption of UV wind lines seen in Be shell stars that are observed from near the disc plane. A key overall result is that, after an initial adjustment to the introduction of the disc, the asymptotic disc destruction rate is typically just an order-unity factor times the stellar wind mass-loss rate. For optically thin Be discs, this leads to a disc destruction time of order months to years, consistent with observationally inferred disc decay times. The much stronger radiative forces of O stars reduce this time to order days, making it more difficult for decretion processes to sustain a disc in earlier spectral types, and so providing a natural explanation for the relative rarity of Oe stars in the Galaxy. Moreover, the decrease in line-driving at lower metallicity implies both a reduction in the winds that help spin-down stars from near-critical rotation, and a reduction in the ablation of any decretion disc; together these provide a natural explanation for the higher fraction of classical Be stars, as well as the presence of Oe stars, in the lower metallicity Magellanic Clouds. We conclude with a discussion of future extensions to study line-driven ablation of denser, optically thick, accretion discs of pre-main-sequence massive stars.

Key words: hydrodynamics – circumstellar matter – stars: early-type – stars: emission-line, Be – stars: mass-loss – stars: winds, outflows.

1 INTRODUCTION

In hot, luminous, massive stars, line scattering of the star's continuum radiation can drive strong stellar wind outflows (Puls, Vink & Najarro 2008). The study here focuses on the role of such line-scattering in driving ablation flows from the surface of circumstellar discs around such massive stars. Such circumstellar discs are observed around both pre-main-sequence (PMS) and main-sequence (MS) massive stars, wherein they respectively act as mediators of mass transfer towards or away from their host star. The high density of PMS accretion discs means that computation of the line-force must account for optically thick continuum transfer, a complication we leave to a follow-up paper (see chapter 7 of Kee 2015).

However, a subpopulation (about 20 per cent; Zorec & Briot 1997) of MS B-stars, the classical Be stars, show doubled peaked Balmer emission lines thought to arise in a circumstellar *decretion* disc, likely formed from orbital ejection of gas from a nearly critically rotating stellar surface (see e.g. Rivinius, Carciofi & Martayan 2013, for general review of Be stars). Observations indicate such Be decretion discs generally have a moderate density (Rivinius et al. 2013), with electron scattering continuum radial optical depths in the disc central plane ranging from marginally optically thin ($\tau \lesssim 1$) to modestly optically thick ($\tau \gtrsim 1$). Since the continuum transfer thus remains optically thin along the bulk of rays impinging the disc at oblique angles, such Be decretion discs provide a natural testbed

★ E-mail: dkee@udel.edu

for exploring line-driven disc-ablation without the added complication of optically thick continuum transfer. Additionally, Be discs are observed to grow and decay on time-scales of months to years, making comparisons of models to observations much more tenable than the comparable project for star-forming discs, which persist for time-scales of thousands of years or more. Finally, as the ubiquitous rapid rotation of classical Be stars is considered to be key to the creation of their discs, these objects provide a natural channel for the extension of this study to include rotational effects.

While observations show $\sim$1/5 of the B stars in our local volume to be Be stars, observations of Oe discs are much less common. In fact, Negueruela, Steele & Bernabeu (2004) suggest that the extension of the classical Be phenomena to O-type stars only continues to spectral type O9 with scattered outliers of earlier special type.[1] Spectropolarimetric observations by Vink et al. (2009) further reinforce the lack of main- or near-MS circumstellar discs around O stars. This break in the appearance of such discs is very evocative and also motivates this work.

Gayley, Owocki & Cranmer (1999) examined line-driven ablation of a static stellar surface by external radiation, e.g. from a close binary companion. In the context of cataclysmic variables, several authors (e.g. Feldmeier & Shlosman 1999; Proga, Stone & Drew 1999) have modelled disc-winds driven by a combination of the disc self-luminosity and line-scattering of radiation from the central white dwarf. In their study of disc angular momentum transport in Be stars, Krtička, Owocki & Meynet (2011) derived scalings for disc ablation, but using flux scalings that ignored Keplerian shear. Gayley, Ignace & Owocki (2001) included such shear in their analysis of how line-forces could induce precession of elliptical orbits in the disc, but they did not study disc ablation.

We focus here on ablation of Be discs, including (as in Proga et al. 1999) all vector components of the line acceleration, accounting for velocity gradients arising both from the wind expansion and the disc shear. We begin in Section 2 by reviewing the relevant background physics including the formalism of line acceleration and the structure of isothermal, circumstellar gaseous discs. Here we also discuss briefly the effects of rapid rotation on stellar shape through oblateness, and stellar brightness through gravity darkening. Section 3 presents simulations of a standard model of a B2 star, including a discussion of the role of stellar rotation in line-driven ablation. This section also presents our parameter study as a function of spectral type. Finally, in Section 4 we summarize the conclusions of this work as well as address potential lines of future work.

2 PHYSICS MODULES AND NUMERICAL SET-UP

2.1 Hydrodynamical equations

We use the PPM (Piecewise Parabolic Method; Colella & Woodward 1984) numerical hydrodynamics code[2] VH-1 to evolve the time-dependent conservation equations for mass and momentum for the changes in time t of the mass density ρ and vector flow velocity $\boldsymbol{v}$,

$$\frac{\partial \rho}{\partial t} + \nabla \cdot (\rho \boldsymbol{v}) = 0, \tag{1}$$

$$\frac{\partial \boldsymbol{v}}{\partial t} + \boldsymbol{v} \cdot \nabla \boldsymbol{v} = -\frac{c_s^2 \nabla \rho}{\rho} - \frac{GM}{r^2}\hat{r} + \boldsymbol{g}_{\rm lines}. \tag{2}$$

For simplicity, we avoid explicit treatment of energy conservation by assuming that the competition between photoionization and radiative cooling maintains a nearly constant gas temperature, taken here to be at the stellar effective temperature, $T = T_{\rm eff}$ (e.g. Drew 1989). This allows us to use the ideal gas law to substitute, within the gas pressure gradient term, for the gas pressure $p = \rho k T/\bar{\mu} = \rho c_s^2$, with k Boltzmann's constant, $\bar{\mu}$ the mean mass per particle, and latter equality defining the isothermal sound speed c_s. Here $\bar{\mu}$ is calculated assuming full ionization at solar abundances. The vector equations are evolved in spherical coordinates $\{r, \theta, \phi\}$, assuming axial symmetry in the ignorable coordinate ϕ.

The right-hand side of equation (2) also includes the vector radiative acceleration from line scattering $\boldsymbol{g}_{\rm lines}$ (discussed further in the next subsection, Section 2.2), and the inward radial stellar gravity[3] at radius r, with G Newton's gravitation constant; here the effective stellar mass $M \equiv M_*(1-\Gamma_e)$ accounts for the reduction in effective gravity by continuum electron scattering opacity κ_e(=0.34 cm^2 g^{-1}), through the ratio of radiative to gravitational acceleration,

$$\Gamma_e \equiv \frac{\kappa_e L_*}{4\pi G M_* c}. \tag{3}$$

2.2 Line acceleration

For the line acceleration, we follow the methodology of (Castor, Abbott & Klein 1975, hereafter CAK) in assuming a power-law distribution in line strength, cast here in terms of the 'quality' of the line resonance (Gayley 1995),

$$q \equiv \frac{\kappa_{\rm L}}{\kappa_e}\frac{v_{\rm th}}{c}, \tag{4}$$

with $v_{\rm th}$ the ion thermal speed, c the speed of light, and $\kappa_{\rm L}$ the line-integrated opacity (measured in units of cm^2 g^{-1}). In this notation, the differential number distribution in line strength is given by

$$\frac{{\rm d}N}{{\rm d}q} = \frac{\bar{Q}}{\Gamma(\alpha) Q_{\rm o}^2}\left(\frac{q}{Q_{\rm o}}\right)^{\alpha-2} e^{-q/Q_{\rm o}}, \tag{5}$$

where α is the power-law index introduced by CAK. Here, the pure CAK power-law distribution is truncated at a maximally strong line of enhancement $Q_{\rm o}$ over continuum opacity, while the normalization $\bar{Q}$ represents the total opacity enhancement in the limit when all the lines are optically thin. For stars with effective temperatures $T_{\rm eff} \gtrsim 30$ kK, $Q_{\rm o} \approx \bar{Q}$ (e.g. Gayley 1995). However, as shown by the NLTE calculations of Puls, Springmann & Lennon (2000), for cooler B stars, $\bar{Q}$ and $Q_{\rm o}$ can differ by factors of a few. Therefore we here use values of Q_0 and $\bar{Q}$ derived by Puls et al. (2000). These line quality parameters are related to the standard CAK line-force normalization by

$$k_{\rm CAK} = \frac{1}{1-\alpha}\left(\frac{v_{\rm th}}{c}\right)^{\alpha} \bar{Q} Q_{\rm o}^{-\alpha}. \tag{6}$$

For a radially accelerating, expanding outflow, all photons only interact with a spectral line at a single resonance location, where the frequency of the photon has been Doppler shifted into the line resonance (Sobolev 1960). For a photon in direction $\hat{\boldsymbol{n}}$, the Sobolev

[1] The earliest type star they found was HD 155806, an O7.5 star. However, the spectral typing of this, and indeed of all Oe stars, is controversial (see e.g. Vink et al. 2009).

[2] http://wonka.physics.ncsu.edu/pub/VH-1/

[3] We ignore self-gravity of the circumstellar material, as it is here many orders of magnitude weaker than that of the central star.

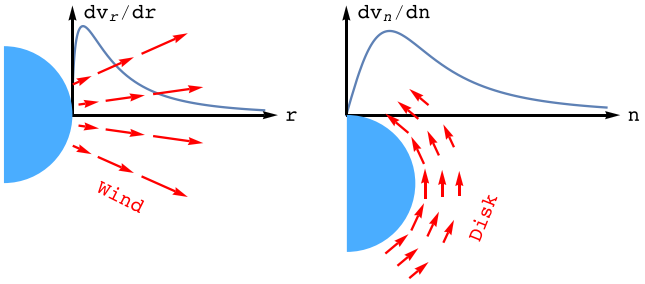

Figure 1. Schematic depiction of the velocity gradient in a radially expanding wind, dv_r/dr (left), and along a non-radial ray direction n through a Keplerian disc with azimuthal shear, dv_n/dn (right).

optical depth across this resonance is, for a line of opacity enhancement q, given by

$$\tau_q(\hat{\boldsymbol{n}}) \equiv \frac{\rho \kappa_e q c}{dv_n/dn}, \tag{7}$$

with the line-of-sight velocity gradient in the $\hat{\boldsymbol{n}}$ direction given by $dv_n/dn \equiv \hat{\boldsymbol{n}} \cdot \nabla(\hat{\boldsymbol{n}} \cdot \boldsymbol{v})$. The associated enhancement of the line acceleration over pure electron scattering is then

$$\frac{g_{\rm line}}{g_e} = q \frac{1 - e^{-\tau_q}}{\tau_q}. \tag{8}$$

For an ensemble of isolated (i.e. non-overlapping) lines, integration over the distribution (5) and the full solid angle of the star with specific intensity $I_*(\hat{\boldsymbol{n}})$ gives for the total line acceleration,

$$\boldsymbol{g}_{\rm lines} = \frac{\kappa_e \bar{Q}}{(1-\alpha)c} \oint \left[\frac{(1+\tau_{\rm o}(\hat{\boldsymbol{n}}))^{1-\alpha} - 1}{\tau_{\rm o}(\hat{\boldsymbol{n}})} \right] I_*(\hat{\boldsymbol{n}}) \hat{\boldsymbol{n}} \, d\Omega, \tag{9}$$

where $\tau_{\rm o}$ is τ_q for $q = Q_{\rm o}$. This is the general, 3D vector form used for the line acceleration calculations in this paper.

In the limit when the strongest line is very optically thick (i.e. $\tau_{\rm o} \gg 1$), the factor in square brackets reduces to $\tau_{\rm o}^{-\alpha}$, giving

$$\boldsymbol{g}_{\rm lines} \approx \frac{\kappa_e \bar{Q}}{(1-\alpha)c(Q_{\rm o}\kappa_e c \rho)^{\alpha}} \oint (\hat{\boldsymbol{n}} \cdot \nabla(\hat{\boldsymbol{n}} \cdot \boldsymbol{v}))^{\alpha} \, I_*(\hat{\boldsymbol{n}}) \hat{\boldsymbol{n}} \, d\Omega. \tag{10}$$

For the classical CAK model with a point star, and so radially streaming photons, the line acceleration is purely radial with a magnitude, $g_{\rm CAK} \propto (dv_{\rm r}/dr)^{\alpha}$, that depends on the radial velocity gradient, $dv_{\rm r}/dr$. In the standard CAK formalism, this line acceleration gives rise to the radial velocity gradients that sustain the self-consistent wind solution.

For an orbiting circumstellar disc, the radial velocity is effectively zero everywhere, implying that the radially streaming photons should impart no line force. However, as illustrated in Fig. 1, the inherent Keplerian shear in the azimuthal orbital velocity of the disc, which declines in radius as $v_\phi \propto 1/\sqrt{r}$, means that non-radial photons see a line-of-sight velocity gradient that desaturates the line-absorption, and so gives rise to a net line force. In the relatively low-density surface layers, the associated acceleration can overcome gravity and lead to a substantial ablation of material from the disc.

To accurately quantify this in a dynamical simulation, it is necessary to account fully for the illumination of the disc by non-radial radiation from the finite angular size of the star. As illustrated in Fig. 2, we have experimented with a range of numerical quadratures for rays that intersect the star with various impact parameters p from the centre, and with various azimuthal angles ϕ', as seen from a given point in the wind. The points on the star are distributed using a Gauss-Legendre quadrature in p^2 and ϕ'. The rays joining

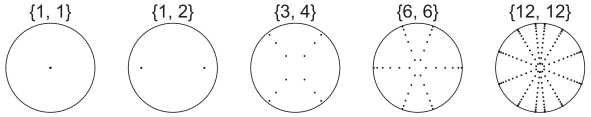

Figure 2. Characteristic ray quadratures for resolving the stellar disc. Each label lists first the number of impact parameters p, and then the number of azimuthal angles ϕ'. This work uses the 6×6 quadrature.

each of the points on the stellar core with the wind reference point then give the line-of-sight directions for calculating the velocity gradients needed in equation (9). The details of the selection of ray quadrature are discussed further in Section 2.5.

In following this standard CAK–Sobolev approach originally developed for a spherically expanding wind, we are assuming that radiation from the stellar core has a single line resonance at any local point where we are computing the line acceleration. However, as discussed in Appendix A, in a configuration with a fast wind at high latitudes and slow or no radial outflow in the equatorial disc, core rays impinging the disc from above and below can sometimes have a *non-monotonic* line-of-sight speed variation, implying then the possibility of *multiple* line resonances.

Any such resonance between the disc viewpoint and the stellar surface can then absorb or scatter the radiation from the stellar core, reducing the local radiative illumination and thus the line-driving of the disc. Moreover, accounting for such 'inner-resonance shadowing' requires in general a global solution of the non-local coupling among all such resonant scattering points, something that would be computationally very costly to incorporate into a hydrodynamical simulation of line-driven disc ablation.

Fortunately, the analysis in Appendix A indicates that, for the continuum optically thin Be discs considered here, the net reduction in line-driving is likely to be less than a factor 2. For computational tractability in this initial study, we thus choose simply to ignore such multiple line resonance effects.

2.3 Stellar rotation

The quadratures above assume the star is spherical, but for rapidly rotating Be stars there can be significant oblateness and associated equatorial gravity darkening. To account for oblateness, we use the formulation of Collins & Harrington (1966), with the standard gravity darkening given by von Zeipel (1924), both of which are succinctly reviewed by Cranmer (1996). The specific rotating model considered has an equatorial surface rotation speed that is 80 per cent of the near surface equatorial orbital speed. This leads to an oblateness characterized by an equatorial to polar radius ratio $r_{*,\rm eq}/r_{*,\rm p} = 1.32$, with an associated ratio of equatorial to polar flux of $F_{\rm eq}/F_{\rm pole} = 0.2$. The rotating models have their surface-integrated flux normalized such that total stellar luminosity is preserved. To enforce this, the quadratures discussed in the previous section are remapped on to an oblate spheroid by numerically determining the angular extent of the star along each of the ϕ' directions used, and then distributing the points in impact parameter over this range. Each ray is then assigned a flux weighting proportional to the effective gravity at its stellar footpoint. As the simulation is isothermal, the associated θ dependence of stellar effective temperature is ignored. For simplicity, the models presented here also ignore limb darkening, but tests we have done show that adding limb darkening leads to less than a 10 per cent reduction in disc mass ablation rate.

2.4 Disc initial condition

To set the initial conditions for our simulations, we first relax a time-dependent wind simulation to a steady state for each case. We then superimpose a simple analytic model of a circumstellar disc, now specified in cylindrical coordinates $\{R, z, \phi\}$, with $R \equiv r \sin\theta$, $z \equiv r\cos\theta$, and again assuming axial symmetry in the ignorable coordinate ϕ. As reviewed by Bjorkman (1997), a geometrically thin, isothermal disc whose vertical extent is controlled by the competition of gas pressure and stellar gravity has a Gaussian vertical structure such that

$$\rho(R, z) = \rho_{\rm eq}(R) \mathrm{e}^{-z^2/2H(R)^2} \tag{11}$$

where the local scaleheight is given by

$$H(R) = \frac{c_{\rm s}}{v_{\rm orb}(R_*)} \frac{R^{3/2}}{R_*^{1/2}}, \tag{12}$$

where $R_* \equiv r_{*,\rm eq}$, and the density in the equatorial plane at cylindrical radius R is assumed to follow a power law,

$$\rho_{\rm eq}(R) = \rho_{\rm o} \left(\frac{R}{R_*}\right)^{-n}. \tag{13}$$

This choice is supported for Be discs by the power-law+Gaussian-disc radiative transfer models of Touhami, Gies & Schaefer (2011). A systematic fitting by Silaj et al. (2010) of H α profiles from the decretion discs of classical Be stars shows that n can vary between[4] 1.5 and 4, with statistically significant peak around $n \approx 3.5$. Since this is also the index found analytically for viscous transport in a decretion disc (Rivinius et al. 2013), and is the favoured choice of fixed n for other classical Be models (e.g. Carciofi et al. 2009), we adopt here $n = 3.5$ for all models.

By taking the steady state form of equations (1) and (2), and the density structure of the disc from equation (13), the approximate azimuthal velocity necessary to centrifugally support the disc is

$$v_\phi(R, z) = \sqrt{\frac{GM_*}{R}} \frac{|z|}{\sqrt{R^2 + z^2}} \sqrt{1 + n\left(\frac{H}{R}\right)^2}. \tag{14}$$

Here, the second term in the radical represents a small radial pressure correction to the standard form of Keplerian orbital velocity, included to create initial conditions as close as possible to a stable equilibrium state.

For opacity arising purely from electron scattering, the radial optical depth through the disc mid-plane is

$$\tau_{\rm disc} = \int_{r_*}^{\infty} \kappa_e \rho_{\rm eq} \mathrm{d}R = \frac{\kappa_e \rho_{\rm o} R_{\rm eq}}{n-1}. \tag{15}$$

To ensure the discs remain marginally optically thin, we set the base density of all models to $\rho_{\rm o} = 1/(\kappa_e R_{\rm eq})$, which gives $\tau_{\rm disc} = 1/(n-1) = 0.4$. For the fully ionized, solar metallicity value $\kappa_e = 0.34$ cm^2 g^{-1} and $R_{\rm eq} = 5R_\odot$ (as used below for the standard B2 model), $\rho_{\rm o} = 8.5 \times 10^{-12}$ g cm^{-3}, within the range of typical values inferred for classical Be stars (see e.g. Rivinius et al. 2013).

Using this base density for the disc, Fig. 3 plots contours for the spatial distribution of log (ρ) for the initial condition of our standard model of a B2e star.

[4] For PMS accretion discs the power-law index is found by Fischer, Henning & Yorke (1996) to be between 0.5 and 2.

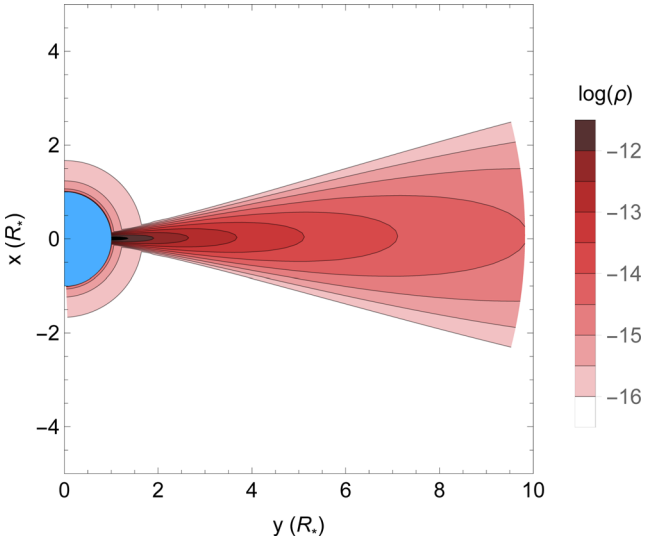

Figure 3. Contours for the spatial distribution of log density (in g cm^{-3}) for the initial condition of our B2e standard model.

Table 1. Grid specifications.

	r	θ
Min.	R_*	0
Max.	10 R_*	π
Number of zones	300	120
Stretch	1.02	1.015
Min. grid spacing	4.7×10^{-4} R_*	1.7×10^{-2} R_*

2.5 Numerical specifications

The simulations here must resolve both the spatial variations of density and velocity in r and θ (or R and z), as well the stellar intensity as a function of impact parameter p and observer centred angular position on the star ϕ'.

As summarized in Table 1, the spatial grid ranges from pole to pole in latitude, and over 1–10 $r_{*,\rm eq}$ in radius, with the highest latitudinal resolution at the equator (to resolve the hydrostatic disc), and the highest radial resolution near the surface (to resolve the steep transition to transonic wind over about an atmospheric scale height). Away from the disc or the stellar surface, the respective grid spacings are increment across each successive zone by the fixed multiplicative 'stretch factors' quoted in Table 1.

For the ray quadrature, ensuring sufficient resolution is less apparent, largely due to the fluctuating small-scale structures generated by ablation. Since each viewing direction shows a different velocity gradient, these small-scale structures can be of different magnitudes and, in some cases, even different positions with changing ray quadratures. The sharp interface between the disc and wind also contributes to significant differences between velocity gradients for neighbouring rays. On a grid level, it is thus difficult to identify a quadrature with clear formal convergence, so a more global criterion is needed. Referring to the testing in Kee (2015), we find that a quadrature with six points in both impact parameter and ϕ' is sufficiently dense to ensure that the quantities of interest, most importantly the rate of disc ablation, are not an artefact of the chosen quadrature.

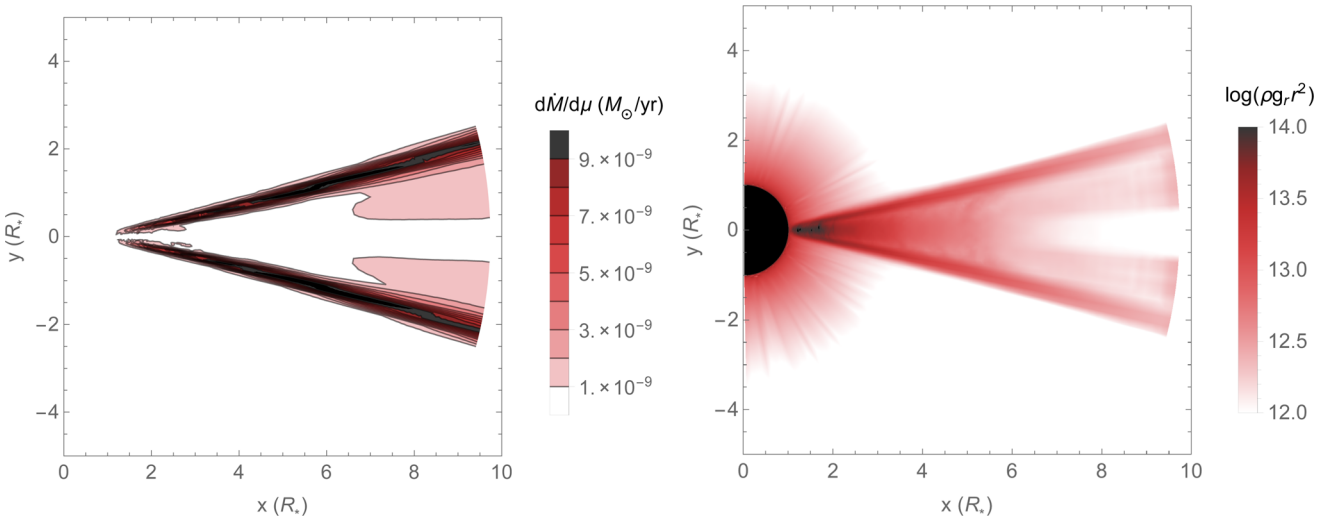

Figure 4. Left: latitudinal distribution of mass-loss $\mathrm{d}\dot{M}/\mathrm{d}\mu$ (equation 16) for the standard B2 model, plotted in units of $\mathrm{M}_\odot\ \mathrm{yr}^{-1}$. Right: force-per-unit-length $\rho g_r r^2$ in cgs units. Both quantities have been time averaged from 1×10^6 to 3×10^6 s to omit the initial interval of disc readjustment to the introduction of radiative forces.

Table 2. Stellar and disc parameters of the B2 standard model.

$T_{\rm eff}$ (kK)	L_* ($\mathrm{L}_\odot$)	M_* ($\mathrm{M}_\odot$)	R_* ($\mathrm{R}_\odot$)	$M_{\rm disc}$ ($\mathrm{M}_\odot$)
22	5.0×10^3	9	5.0	1.9×10^{-10}

Table 3. Wind parameters of the B2 standard model.

$\bar{Q}$	$Q_{\rm o}$	α	$\dot{M}_{\rm wind}$ ($\mathrm{M}_\odot\ \mathrm{yr}^{-1}$)
1800	4900	0.59	5.8×10^{-10}

For boundary conditions at the poles, we enforce standard axisymmetry. At the stellar base, we assume a fixed density[5] independent of latitude, and set the radial velocity by linear extrapolation, with the constraint that $|v_{\rm r}| \leq c_{\rm s}$. We also impose zero latitudinal velocity, and azimuthal velocity set by the stellar rotation at this boundary. At the outer boundary, we use a simple extrapolation assuming a zero radial gradient in all quantities. This allows for simple outflow in the wind regions, while keeping any outer oscillations in the disc to a small amplitude.

3 RESULTS

3.1 Model of a non-rotating B2 star

For our standard model, we choose a B2 star both because of its moderately strong luminosity and also because this is near the spectral type with the largest fraction of Be stars. Table 2 provides the full set of stellar and disc parameters as derived from the evolutionary tracks of Georgy et al. (2013) and the effective temperature calibrations of Trundle et al. (2007). Table 3 gives the wind parameters as derived by Puls et al. (2000).

For this non-spherical but azimuthally symmetric simulation, the latitudinal distribution of mass-loss can be characterized by

$$\frac{\mathrm{d}\dot{M}}{\mathrm{d}\mu} \equiv 2\pi\rho v_{\rm r} r^2, \tag{16}$$

where $\mu \equiv \cos\theta$. The left-hand panel of Fig. 4 plots the time average of this quantity from $t = 10^6$ to 3×10^6 s, well after the adjustment of the simulation from its initial conditions. The results vividly illustrate that ablation mostly occurs in thin layers along the upper and lower edges of the disc.[6]

To illustrate the dynamical driving associated with this ablation, the right-hand panel of Fig. 4 plots the log of the radial force-per-unit-radius, $\rho g_r r^2$. Note that the ablated material is accelerated throughout the full radius, but since the opening angle of the layer remains nearly constant in radius, we interpret this as continuing acceleration of the material that has been dislodged from the disc near the star, rather than an addition of new disc material to the ablation flow.

This interpretation is supported by comparison of density snapshots from each model as a function of time. As illustrated in Fig. 5, the disc is removed from its inner edge outwards. Additionally, as shown in Fig. 6, the radial velocity is negligible in the bulk of the disc, but reaches a few hundred km s^{-1} within thin wind–disc boundary layers corresponding to those shown in Fig. 4. Observationally, this implies emission lines of classical Be stars should decay most rapidly in their outer wings, where emission comes from the highest orbital velocities near the stellar surface. It also suggests that the Doppler shift with respect to line centre of classical Be star emission lines should remain approximately constant throughout the decay, as this is set by the outer disc edge, which remains relatively unperturbed throughout much of the ablation process.

While the disc ablation is strong in thin surface layers of the disc, when integrated over solid angle the associated mass-loss is only a factor of a few higher than that of the steady-state wind. Fig. 7 quantifies this by plotting three different characterizations

[5] This base density is $\rho_* = 5\rho_{\rm sonic}$, with $\rho_{\rm sonic} \equiv \dot{M}_{\rm CAK}/(4\pi r_{\rm sonic}^2 c_{\rm s})$ the density at the sonic radius $r_{\rm sonic}$, where $v_{\rm r}(r_{\rm sonic}) = c_{\rm s}$. Here $\dot{M}_{\rm CAK}$ refers to the analytic CAK mass-loss rate including the finite disc correction factor. For this B2 model, $\rho_* = 5 \times 10^{-14}$g cm s^{-3}.

[6] The small pink excursions into the central region of the disc are the remnants of small-scale oscillatory motions set off by the relaxation of the initial conditions. Elsewhere in the disc, these have averaged out.

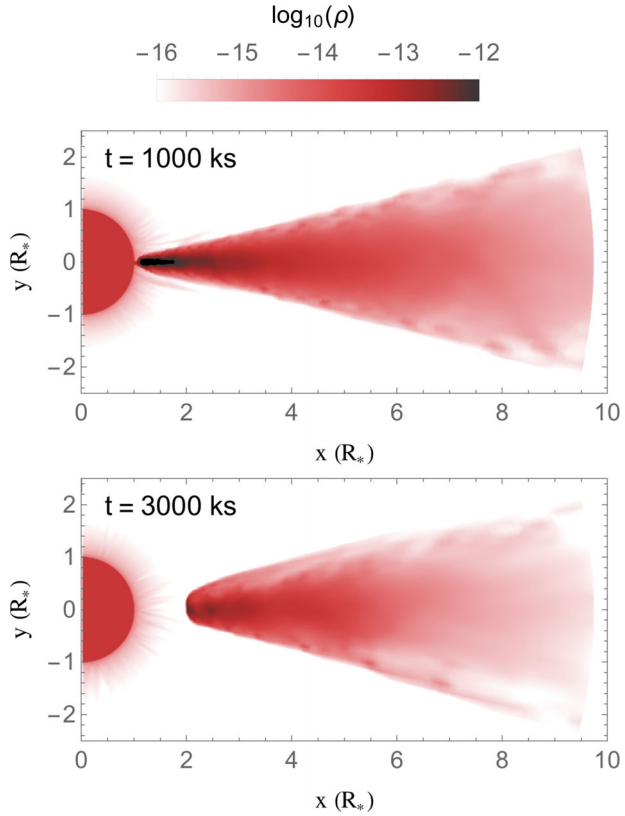

Figure 5. Snapshots of log density for the B2 model at times $t = 1000$–3000 ks from the initial condition, showing the removal of the disc from the stellar surface outwards.

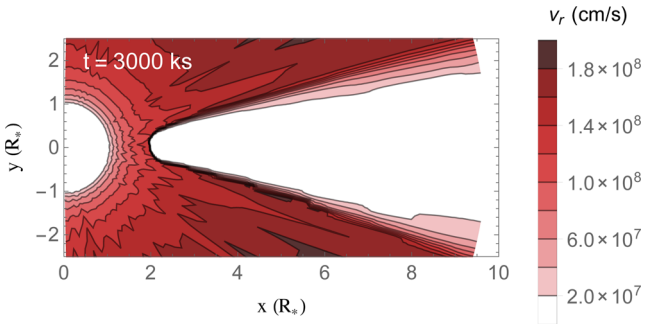

Figure 6. Snapshot of radial velocity for the B2 model at time $t = 3000$ ks from the initial condition, emphasizing the thinness of the slow-moving ablation layers, with $v_r \sim 100$ km s^{-1}.

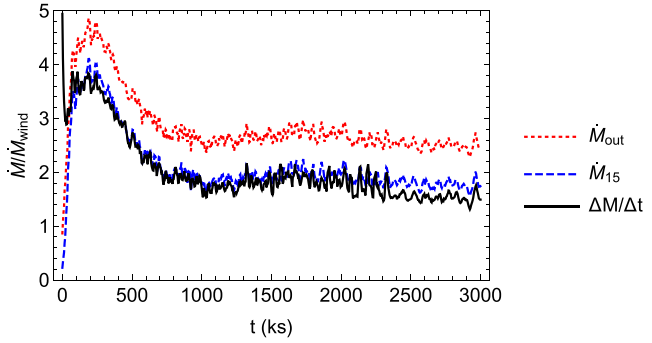

Figure 7. Mass-loss rate (win units of spherically symmetric wind mass-loss rate) for three mass-loss metrics of the standard model of a B2 star.

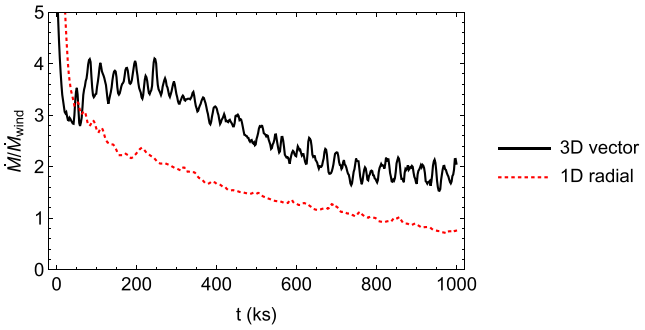

Figure 8. Ablation rate, measured in units of the spherically symmetric mass-loss rate, for the two force implementations discussed in the text.

of the simulation mass-loss, normalized by the steady-state wind rate. The uppermost curve, labelled $\dot{M}_{\rm out}$, is the total mass-loss rate through the outer boundary, while $\dot{M}_{15}$ represents the outer boundary mass-loss in a band of $\pm 15^\circ$ above and below the equator. The latter is quite comparable to the total rate of change of mass in the simulation,[7] $\Delta M/\Delta t$, indicating that both these are good representations of the total disc ablation rate, with little contribution from the steady wind. After an initial adjustment, the disc ablation rate settles down to about two times the wind mass-loss rate. The small difference towards the final time between $\dot{M}_{15}$ and $\Delta M/\Delta t$ can be accounted for by the shrinking of solid angle of the disc and the contamination of $\dot{M}_{15}$ by wind mass-loss. In the following, we use $\Delta M/\Delta t$ as the best characterization of disc ablation rate.

3.2 Importance of non-radial velocity gradients

While the full results presented in the rest of this paper use the complete 3D vector acceleration described in Section 2.2, it is instructive for testing to examine reduced models that assume $\boldsymbol{v}(r) = v_{\rm r}\hat{\boldsymbol{r}}$ and $v_\theta = v_\phi = \partial v_{\rm r}/\partial\theta = \partial v_{\rm r}/\partial\phi = 0$ in computing a purely radial[8] line acceleration $\boldsymbol{g} = g_r\hat{\boldsymbol{r}}$. Since such conditions do apply in the high-latitude wind, we expect the wind to be unchanged among the three implementations, and this comparison can test the importance of the non-radial velocity gradient terms in causing ablation. It can also help disentangle what portion of the mass lost from the disc is due to ablation – by which we mean the removal of material only by direct acceleration of disc material by radiation – and what fraction is from 'entrainment', wherein the wind drags away low-density disc material viscously coupled through a Kelvin–Helmholtz instability. Fig. 8 shows that, asymptotically, the 3D vector form yields a disc ablation rate more than twice the 1D radial model. Thus, we can infer that, while the strong velocity shear between wind and disc does indeed entrain material, this contributes at most half of the total disc ablation rate.

3.3 Sample comparison with IUE spectrum of Be shell star

This strong concentration of mass ablation along the surface layers of the disc seems qualitatively what is needed to explain the blueshifted absorption troughs seen in IUE spectra of UV wind lines

[7] The initial spike in the rate of change of mass in the simulation is due to mass falling back on to the star during the adjustment phase.
[8] This is achieved by replacing $\hat{\boldsymbol{n}} \cdot \nabla(\hat{\boldsymbol{n}} \cdot \boldsymbol{v})$ with $\mu^2 {\rm d}v_{\rm r}/{\rm d}r + (1-\mu^2)v_{\rm r}/r$ in equation (10).

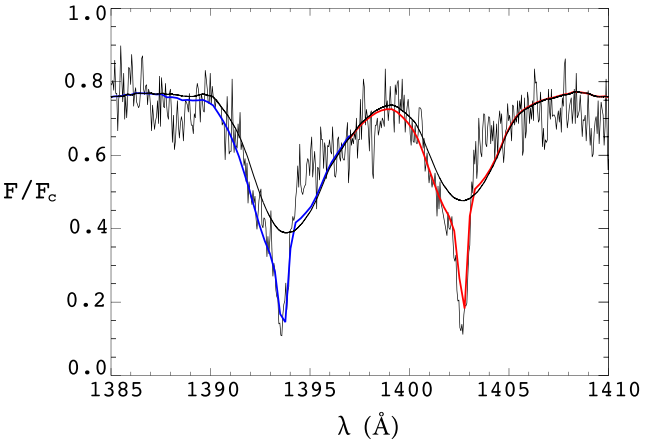

Figure 9. IUE flux spectrum for the Si IV line doublet of the Be shell star ϕ Per, overplotted versus wavelength (in Å) with synthetic line profiles. The black curve showing broad, shallow absorption is for photospheric profiles from TLUSTY (Lanz & Hubeny 2007) for the star's spectral type (B2Ve; Lesh 1968), rotationally broadened according to the star's Vsini = 450 km s^{-1} (Abt, Levato & Grosso 2002). The deeper, narrow absorption troughs show the blue/red components of the Si IV doublet, computed from applying a UV line-synthesis code for our B2 disc ablation model, viewed from 6 deg above the equator. The IUE continuum is reduced by a factor 0.8 to account for line blanketing in the synthetic pseudo-continuum.

(e.g. Si IV) from Be shell stars that are observed from near the equatorial plane (Grady, Bjorkman & Snow 1987). Preliminary calculations we have performed with a multidimensional UV line synthesis code described in Nazé et al. (2015) indeed show that these models can match quite well UV line profiles from IUE spectra of specific Be shell stars; Fig. 9 shows a sample with $\langle q\dot{M}\rangle = 1.6 \times 10^{-11}$, where q is the ion-fraction of Si IV and $\dot{M}$ is the spherically symmetric mass-loss rate of the model (see e.g. Nazé et al. 2015). In preliminary calculations, both the depth of the line and its extent bluewards of line-centre depend on the viewing angle, with changes of 3° in viewing angle causing 15–20 per cent changes in depth of the line and as much as order unity changes in the line width. However, because fits involve adjustment of several parameters (e.g. for ionization fraction, macro- and microturbulence, viewing angle, etc.), we defer a detailed discussion to a future paper.

3.4 Model of a rotating B2 star

Recalling that rapid rotation is a ubiquitous feature of classical Be stars, let us next examine the effect of rapid rotation, and the associated stellar oblateness and gravity darkening, on line-driven ablation. For this, we modify our standard B2 model to have $W = v_{\rm rot}/v_{\rm orb} = 0.8$. Stellar structure dictates that rapid rotation would cause the equatorial radius to swell, leaving the polar radius nearly unchanged. Instead, to isolate the effect of gravity darkening and provide a direct comparison with equatorial disc ablation of a non-rotating model, we here keep the equatorial radius fixed, and so now require the polar radius to shrink. This means that the rotating and non-rotating models have the same mass and equatorial radius, and thus the same equatorial escape speed. Fig. 10 shows the initial condition superposition of a disc on a relaxed, steady state, rotating wind. Note now the equatorial oblateness of the underlying star, with however a bipolar enhancement of the wind density, reflecting the stronger mass-loss from the gravity-brightened poles.

Fig. 11 compares the ablation rate of the models with and without rotation, showing that equatorial gravity darkening modestly

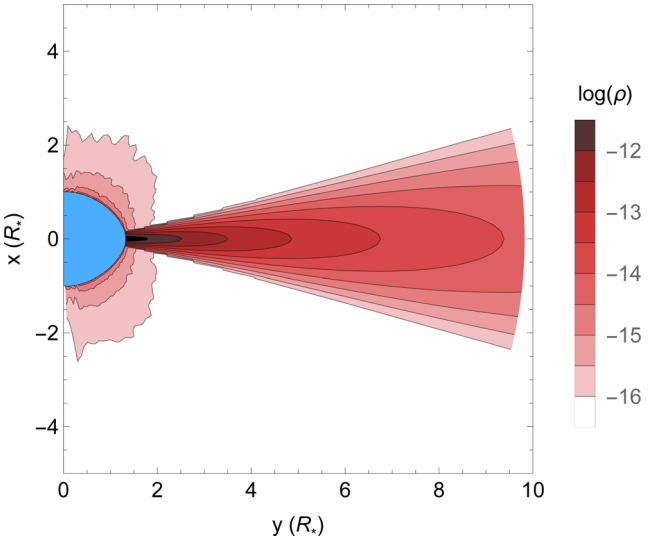

Figure 10. Initial condition of the rotating B2 model, plotted in log density, in g cm^{-3}.

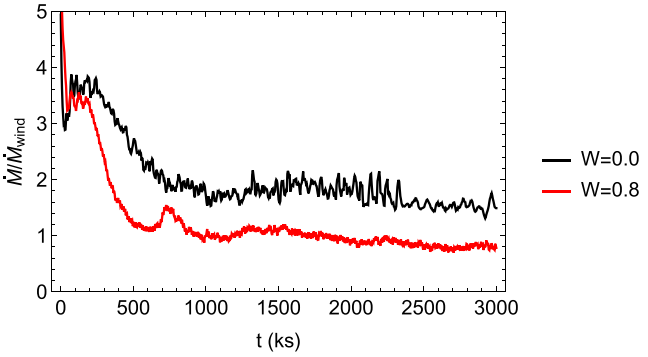

Figure 11. Time evolution of disc ablation rate for both the rotating ($W = 0.8$) and non-rotating ($W = 0.0$) B2 model, in units of the associated steady-state wind mass-loss rates (which is about 6 per cent higher for the non-rotating model).

reduces the disc ablation rate, by a maximum factor about 2. Following the review by Cranmer (1996), this is consistent with the comparable factor 2 reduction in equatorial surface brightness between the non-rotating and rotating models, due to this gravity darkening. Keeping the equatorial radius constant removes the attendant reduction of equatorial escape speed normally associated with rapid rotation. Therefore, this choice maximizes the difference between the ablation of the rotating and non-rotating models. In addition, both modern theoretical analyses (see e.g. Espinosa Lara & Rieutord 2011) and recent interferometric observations (Domiciano de Souza et al. 2014) suggest a gravity darkening exponent lower than the value 0.25 derived by von Zeipel (1924); adopting such a lower exponent would moderate the effect of gravity darkening on line-driven ablation. Taken together, the lower equatorial escape speed and higher equatorial brightness should lead to an ablation rate somewhere between the lower limit presented here and the ablation rate of a non-rotating star.

3.5 Ablative destruction of a disc around an O7 star

As discussed above, the incidence of the Be phenomena peaks around spectral type B2 and declines towards earlier spectral types,

Table 4. Stellar and disc parameters of the O7 model.

$T_{\rm eff}$ (kK)	L_* ($L_\odot$)	M_* ($M_\odot$)	R_* ($R_\odot$)	$M_{\rm disc}$ ($M_\odot$)
36	1.3×10^5	26.5	9.4	7.0×10^{-10}

Table 5. Wind parameters of the O7 model.

$\bar{Q}$	$Q_{\rm o}$	α	$\dot{M}_{\rm wind}$ ($M_\odot$ yr^{-1})
2500	2200	0.66	1.5×10^{-7}

with only a few detected O9e stars in the Milky Way. While the exact mechanism for ejection of material into a circumstellar decretion disc is uncertain, we can address here how long such a circumstellar disc can survive the stronger radiative ablation associated with the greater luminosity of such earlier type stars. To quantify this, we now present a simulation of the ablation of a marginally optically thin disc around an O7 star, with star, disc, and wind parameters given by Tables 4 and 5 as taken from Martins, Schaerer & Hillier (2005) and Puls et al. (2000). The choice of keeping the disc marginally optically thin leads to a factor 5 increase in disc mass, but the factor 25 higher luminosity leads to a factor 200 increase in the wind mass-loss rate. Therefore, we should expect much stronger disc ablation.

Indeed, instead of the gradual disc surface ablation found for the B2 star case, Fig. 12 shows that radiative acceleration of an O7 star is strong enough to simply drive away the entire disc over a dynamical time-scale. To quantify further the evolution of the disc material for this O7-star case, Fig. 13 plots the spatial and temporal variation of the mass in each spherical shell,

$$\frac{{\rm d}M}{{\rm d}r} \equiv \oint \rho r^2 {\rm d}\Omega. \qquad (17)$$

Note particularly the rapid removal of material from the inside of the disc outwards, as well as the quite short (∼3 d) time it takes for the disc to be completely evacuated.

The brown curve in Fig. 14 plots the time variation of the total, wind-normalized ablation rate for this O7 simulation. Whereas the B2 model (black curves) slowly relaxes to a relatively steady ablation rate about twice the wind mass-loss rate, the O7 model impulsively ejects the disc material in a sustained burst, leaving finally only a steady-state wind. This removal of the disc is so sudden that the ablation rate never significantly exceeds the spherically symmetric mass-loss rate.

We thus see that an O7 star destroys a pre-existing optically thin disc on a dynamical time-scale. To counter this destruction, the star would need to feed a disc at a rate of over $1.5 \times 10^{-7} M_\odot$ yr^{-1}. This is so much larger than that needed to maintain a disc for later spectral types, and so provides a natural explanation for why there are no galactic O7e stars (see e.g. Martayan et al. 2006; Rivinius et al. 2013).

3.6 Ablation as a function of spectral type

To bridge between the gradual surface ablation seen for the B2 model and the dynamic disc ejection seen for the O7 star, let us now consider intermediate spectral types, with parameters given in Tables 6 and 7. For the O stars stellar parameters are taken from Martins et al. (2005) while, as was done for the B2 star, Trundle et al. (2007) and Georgy et al. (2013) are used for the B stars. Puls et al. (2000) is used for all wind parameters.

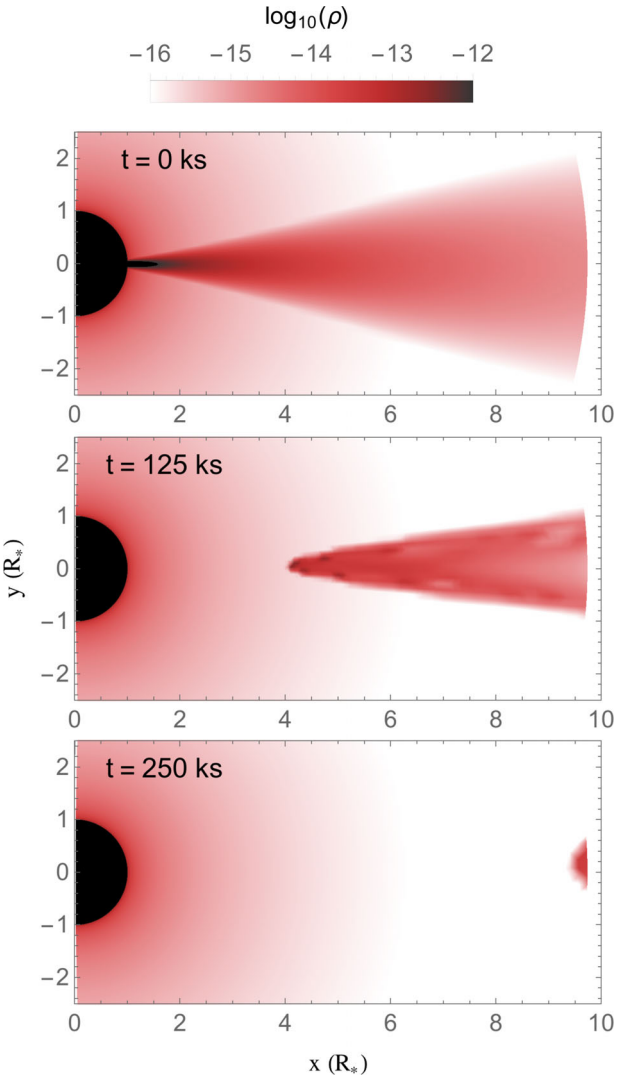

Figure 12. Snapshots of log density for the O7 model at times $t = 0$, 125, and 250 ks from the initial condition, showing now the rapid destruction of the initial disc on a dynamical time-scale by the strong radiation field of the O7 star.

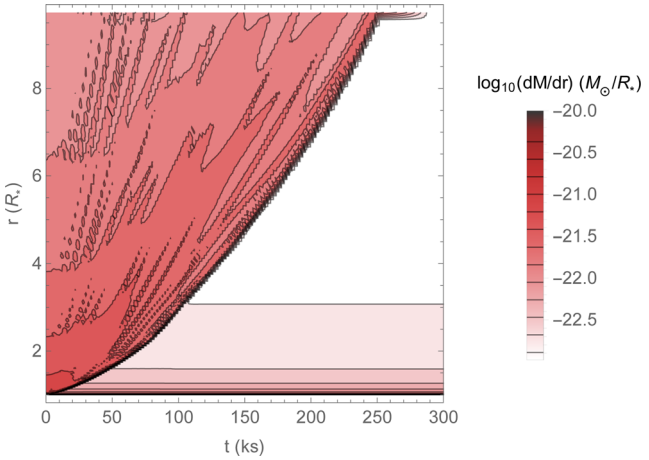

Figure 13. For the O7 model, time evolution of dM/dr (defined in equation 17), the mass in spherical shells above the stellar surface, in units of solar masses per stellar radius.

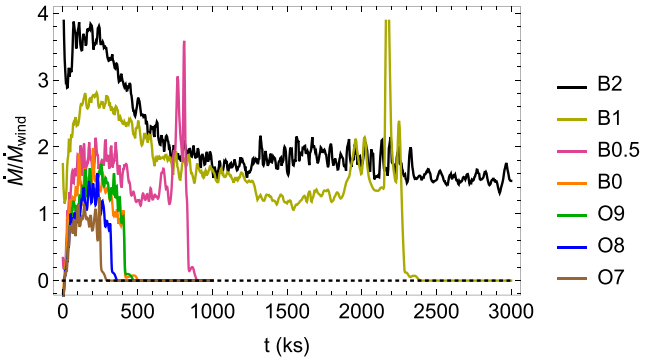

Figure 14. For various spectral types as labelled, the time evolution the disc ablation rate, measured in units of the corresponding spherically symmetric wind mass-loss rate $\dot{M}_{\rm wind}$ for each spectral type.

Table 6. Stellar and disc parameters as a function of spectral type.

Sp. type	$T_{\rm eff}$ (kK)	L_* ($L_\odot$)	M_* ($M_\odot$)	R_* ($R_\odot$)	$M_{\rm disc}$ ($M_\odot$)
B3V	18	1.6×10^3	6	4.1	1.3×10^{-10}
B2V	22	5.0×10^3	9	5.0	1.9×10^{-10}
B1V	24	7.9×10^3	11	5.2	2.0×10^{-10}
B0.5V	28	1.6×10^4	13	5.5	2.3×10^{-10}
B0V	31	1.6×10^4	16	6.0	2.7×10^{-10}
O9V	32	5.0×10^4	18	7.7	4.8×10^{-10}
O8V	33	7.9×10^4	22	8.5	5.7×10^{-10}
O7V	36	1.3×10^5	26.5	9.4	7.0×10^{-10}

Table 7. Wind parameters as a function of spectral type.

Sp. type	$\bar{Q}$	$Q_{\rm o}$	α	$\dot{M}_{\rm wind}$ ($M_\odot$ yr^{-1})
B3V	1500	7000	0.55	6.6×10^{-11}
B2V	1800	4900	0.59	5.8×10^{-10}
B1V	2000	4600	0.60	1.5×10^{-9}
B0.5V	2300	3900	0.63	5.7×10^{-9}
B0V	2400	3400	0.64	1.9×10^{-8}
O9V	2400	3300	0.65	3.6×10^{-8}
O8V	2300	3100	0.65	6.9×10^{-8}
O7V	2200	2500	0.66	1.5×10^{-7}

Given the stellar radius and mass, the base disc density is again set to keep the disc marginally thin, with a fixed radial optical depth $\tau_{\rm disc} = 0.4$. Upon integration over the full simulation volume, the scaling of the disc mass is then given by

$$M_{\rm disc} = \frac{(2\pi)^{3/2}}{\kappa_e} \frac{a}{\sqrt{G M_*}} R_*^{2.5} \ln(10)$$
$$= 1.24 \times 10^{-10}\,{\rm M}_\odot \sqrt{\frac{T}{10^4\,{\rm K}}} \sqrt{\frac{10\,{\rm M}_\odot}{M}} \left(\frac{R}{5\,{\rm R}_\odot}\right)^{2.5}. \quad (18)$$

For the various spectral types, Fig. 14 compares the time evolution of the wind-scaled disc ablation rate. This highlights two populations. (1) Stars B0 and earlier behave like the O7 star, and dynamically eject their disc in a time $t \lesssim 5 \times 10^5$ s. (2) Stars later than B0 behave like the B2 star, with an interval of steady, slow ablation at a rate comparable to the wind mass-loss, terminating in a mass-loss burst as the final portion of the disc is removed.

In Fig. 15, the black circles plot the disc destruction time for each of the various spectral types. These follow closely the simple scaling given by the ratio of the initial disc mass to wind mass-loss rate $M_{\rm disc}/\dot{M}_{\rm wind}$, shown in red squares. This suggests that this

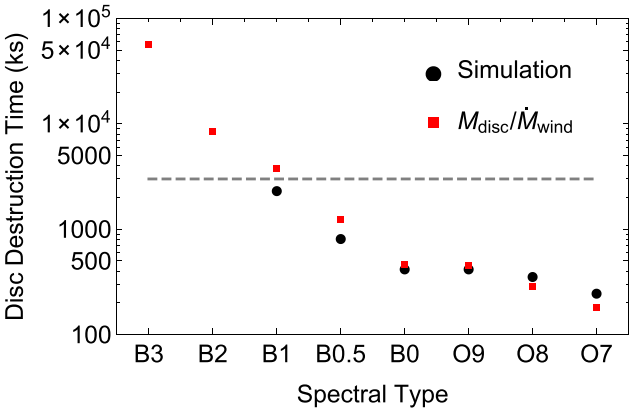

Figure 15. Time to destroy an optically thin disc as predicted by $M_{\rm disc}/\dot{M}_{\rm wind}$ (red squares) compared with the time it actually takes in the simulations (black circles). The dashed line denotes the duration of the longest simulation, meaning no simulations have been run long enough to see the disc removal completed for the B2 or B3 case.

simple scaling form can be generally used to predict disc destruction times, even for later spectral types and longer simulation times than considered here. Since the disc mass diverges only logarithmically with outer disc radius, increasing the simulation volume will increase the disc mass, and thus the disc destruction time, by an order unity factor at most. However, as most classical Be stars have emitting regions inferred to be on the order of, or less than, $10R_*$ (see e.g. Meilland et al. 2012; Touhami et al. 2013), and since disc removal occurs from the inner edge outwards, the time-scales presented here will still provide a good estimate of the time for circumstellar emission to disappear.

The ability of this simple scaling to predict simulation results guides its use to predict the behaviour of actual Be stars. Previous work by Carciofi et al. (2012) observationally inferred a disc decay for the Be star 28 CMa of order a half year. To reproduce this disc decay time within the standard viscous diffusion model, these authors invoked a viscosity coefficient[9] $\alpha \approx 1$ (Shakura & Sunyaev 1976). By comparison, simulations of the magnetorotational instability, thought to be the origin of viscous transport in ionized gaseous discs, show a much lower value, $\alpha \lesssim 0.01$ (see e.g. Papaloizou & Nelson 2003), implying then a much longer diffusive decay time. The inferred stellar parameters of 28 CMa from Maintz et al. (2003) are very similar to the B2 model, for which the predicted ablative disc destruction time is within a factor of 2 of the observationally inferred disc decay time.

This important result suggests that line-driven ablation can readily explain the relatively short, few-month time-scale observationally inferred for Be-disc decay, without the need to invoke anomalously strong viscous diffusion.

4 SUMMARY AND FUTURE WORK

The study here has carried out detailed multidimensional radiation-hydrodynamical simulations of line-driven ablation of optically thin discs around luminous, early-type stars. A key general result is that the disc mass ablation rate scales closely, within a factor of a few, with the global mass-loss rate of the steady-state stellar wind, implying that the disc destruction time-scale can be characterized by

[9] Reanalysis of the data suggests a potential modest reduction to $\alpha \approx 0.4$ (Carciofi, private communication).

the simple ratio of disc mass to steady-state wind mass-loss rate, $M_{\rm disc}/\dot{M}_{\rm wind}$. For O stars, this implies disc destruction on a dynamical time-scale, thus helping to explain the relative rarity of classical Oe stars. For Be stars, the destruction takes much longer than the dynamical time-scale, but is still much shorter than a characteristic viscous diffusion time, thus helping to explain the inferred rapid decay of Be discs without having to appeal to anomalously strong viscous diffusion.

In the context of Be stars, future work should apply the results and scalings derived here to other cases where there is disc decay after a presumed cessation of the processes that feed the disc. More generally, however, future work should seek to identify mechanisms for disc feeding, perhaps through mass ejection induced by stellar pulsations (see Kee et al. 2014), and couple these with simulations of disc decay through radiative ablation. As discussed in Section 3.3, a detailed comparison of synthetic and observed UV line profiles from Be shell stars can provide direct diagnostic constraints on the disc surface ablation models computed here.

Future work can also extend these results to lower metallicity environments. The Magellanic Clouds show a higher fraction of Be stars (e.g. Martayan et al. 2006, 2007), with the classical Be phenomenon also extending to much earlier spectral types than in the Milky Way (Golden-Marx et al. 2016). In the context of line-driven disc ablation, these differences could be a natural consequence of the lower metallicity and attendant lower effective opacity in UV metal ion lines. It is well established both observationally and theoretically (e.g. Vink, de Koter & Lamers 2001; Mokiem et al. 2007) that line-driven winds are weaker at lower metallicities, and, given the results presented here, we can expect weaker disc ablation in the lower metallicity Magellanic Clouds.

In a broader context of accretion discs from PMS stars, a key need is to generalize the above models to account for the effects of significant continuum absorption and scattering in their denser, optically thick discs, where cooling to temperatures significantly below $T_{\rm eff}$ will also occur. This will allow exploration of the role of line-scattering accelerations in mass accretion and massive star formation. These results could even have potential implications for controlling the stellar upper mass limit.

ACKNOWLEDGEMENTS

We acknowledge use of the VH-1 hydrodynamics code, developed by J. Blondin and collaborators. This work was supported in part by NASA ATP grant NNX11AC40G and NASA Chandra grant TM3-14001A, awarded to the University of Delaware. JOS acknowledges funding from the European Union's Horizon 2020 research and innovation programme under the Marie Sklodowska-Curie grant agreement no. 656725. Finally, we acknowledge many helpful comments and constructive criticisms from the anonymous referee.

REFERENCES

Abt H. A., Levato H., Grosso M., 2002, ApJ, 573, 359
Bjorkman J. E., 1997, in De Greve J. P., Blomme R., Hensberge H., eds, Lecture Notes in Physics, Vol. 497, Stellar Atmospheres: Theory and Observations. Springer-Verlag, Berlin, p. 239
Carciofi A. C., Okazaki A. T., Le Bouquin J.-B., Štefl S., Rivinius T., Baade D., Bjorkman J. E., Hummel C. A., 2009, A&A, 504, 915
Carciofi A. C., Bjorkman J. E., Otero S. A., Okazaki A. T., Štefl S., Rivinius T., Baade D., Haubois X., 2012, ApJ, 744, L15
Castor J. I., Abbott D. C., Klein R. I., 1975, ApJ, 195, 157 (CAK)
Colella P., Woodward P. R., 1984, J. Comput. Phys., 54, 174
Collins G. W., II, Harrington J. P., 1966, ApJ, 146, 152
Cranmer S. R., 1996, PhD thesis, Univ. Delaware
Domiciano de Souza A. et al., 2014, A&A, 569, A10
Drew J. E., 1989, ApJS, 71, 267
Espinosa Lara F., Rieutord M., 2011, A&A, 533, A43
Feldmeier A., Shlosman I., 1999, ApJ, 526, 344
Fischer O., Henning T., Yorke H. W., 1996, A&A, 308, 863
Gayley K. G., 1995, ApJ, 454, 410
Gayley K. G., Owocki S. P., Cranmer S. R., 1999, ApJ, 513, 442
Gayley K. G., Ignace R., Owocki S. P., 2001, ApJ, 558, 802
Georgy C., Ekström S., Granada A., Meynet G., Mowlavi N., Eggenberger P., Maeder A., 2013, A&A, 553, A24
Golden-Marx J. B., Oey M. S., Lamb J. B., Graus A. S., White A. S., 2016, ApJ, 819, 55
Grady C. A., Bjorkman K. S., Snow T. P., 1987, ApJ, 320, 376
Kee N. D., 2015, Dissertation, Univ. Delaware
Kee N. D., Owocki S., Townsend R., Müller H.-R., 2014, preprint (arXiv:e-prints)
Krtička J., Owocki S. P., Meynet G., 2011, A&A, 527, A84
Lanz T., Hubeny I., 2007, ApJS, 169, 83
Lesh J. R., 1968, ApJS, 17, 371
Maintz M., Rivinius T., Štefl S., Baade D., Wolf B., Townsend R. H. D., 2003, A&A, 411, 181
Martayan C., Frémat Y., Hubert A.-M., Floquet M., Zorec J., Neiner C., 2006, A&A, 452, 273
Martayan C., Frémat Y., Hubert A.-M., Floquet M., Zorec J., Neiner C., 2007, A&A, 462, 683
Martins F., Schaerer D., Hillier D. J., 2005, A&A, 436, 1049
Meilland A., Millour F., Kanaan S., Stee P., Petrov R., Hofmann K.-H., Natta A., Perraut K., 2012, A&A, 538, A110
Mokiem M. R. et al., 2007, A&A, 473, 603
Nazé Y., Sundqvist J. O., Fullerton A. W., ud-Doula A., Wade G. A., Rauw G., Walborn N. R., 2015, MNRAS, 452, 2641
Negueruela I., Steele I. A., Bernabeu G., 2004, Astron. Nachr., 325, 749
Papaloizou J. C. B., Nelson R. P., 2003, MNRAS, 339, 983
Proga D., Stone J. M., Drew J. E., 1999, MNRAS, 310, 476
Puls J., Springmann U., Lennon M., 2000, A&AS, 141, 23
Puls J., Vink J. S., Najarro F., 2008, A&AR, 16, 209
Rivinius T., Carciofi A. C., Martayan C., 2013, A&AR, 21, 69
Shakura N. I., Sunyaev R. A., 1976, MNRAS, 175, 613
Silaj J., Jones C. E., Tycner C., Sigut T. A. A., Smith A. D., 2010, ApJS, 187, 228
Sobolev V. V., 1960, Moving Envelopes of Stars. Harvard Univ. Press, Cambridge
Touhami Y., Gies D. R., Schaefer G. H., 2011, ApJ, 729, 17
Touhami Y. et al., 2013, ApJ, 768, 128
Trundle C., Dufton P. L., Hunter I., Evans C. J., Lennon D. J., Smartt S. J., Ryans R. S. I., 2007, A&A, 471, 625
Vink J. S., de Koter A., Lamers H. J. G. L. M., 2001, A&A, 369, 574
Vink J. S., Davies B., Harries T. J., Oudmaijer R. D., Walborn N. R., 2009, A&A, 505, 743
von Zeipel H., 1924, MNRAS, 84, 665
Zorec J., Briot D., 1997, A&A, 318, 443

APPENDIX A: MULTIPLE LINE RESONANCES

A1 Analytic wind+disc velocity model

For our models of a fast stellar wind at high latitudes and a equatorial Keplerian disc with reduced or no radial expansion, lines of sight from the stellar surface towards and/or through the disc can have a non-monotonic line-of-sight velocity, potentially leading then to multiple Sobolev line resonances with equal line-of-sight speed. To characterize the potential effect of shadowing by a more inward resonance on the radiative driving within or near the surface of the equatorial disc, let us consider here a simplified analytic form for such a disc+wind model.

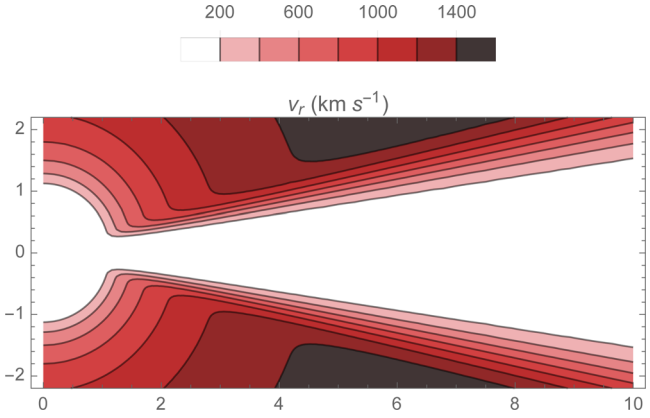

Figure A1. Contours of the spatial variation of radial velocity v_r for analytic wind+disc model with parameters $\theta_d = 12°$, $\Delta\theta = 4°$ and $V_{\infty,o} = 1800$ km s^{-1}, chosen to correspond roughly to the velocity variation in the simulation snapshot shown in Fig. 6.

Specifically, in terms of the radius r and latitude[10] θ, let us assume the radial component the flow speed v_r follows a simple variation[11] from the surface radius r_*,

$$v_r(r,\theta) = V_\infty(\theta)\left(1 - \frac{r_*}{r}\right), \tag{A1}$$

with however a terminal speed $V_\infty(\theta)$ that has a fixed high value $V_{\infty,o}$ over the poles, but then declines steeply near the disc, approaching zero at the equatorial mid-plane. Specifically, for a disc–wind boundary of half-width $\Delta\theta$ centred on latitudes $\pm\theta_d$, we take

$$V_\infty(\theta) = V_{\infty,o}\,\frac{1}{2}\mathrm{Erfc}((\theta_d - |\theta|)/\Delta\theta). \tag{A2}$$

To approximate the velocity form given in Fig. 6 for an actual simulation snapshot, we take here $\theta_d = 12°$, $\Delta\theta = 4°$ and $V_{\infty,o} = 1800$ km s^{-1}; Fig. A1 then shows that the radial velocity in this analytic model has a similar form to that of the numerical simulation snapshot in Fig. 6.

The disc component is taken to have an azimuthal speed given by the Keplerian form for equatorial orbit,

$$v_\phi(r,\theta) = V_{\rm orb}\sqrt{\frac{r_*}{r\cos\theta}}, \tag{A3}$$

where $V_{\rm orb} = \sqrt{GM/r_*}$ is the orbital speed at the equatorial surface radius r_*, taken here to be a third of the polar wind speed, i.e. $V_{\rm orb} = 600$ km s^{-1}.

A2 Projected velocity gradient and shadowing by an inner resonance

Let us now consider conditions at some fixed wind+disc position with radius r_p and co-latitude θ_p. For a near-star position $r_p = 2\,r_*$ in the wind–disc boundary layer with $\theta_p = \theta_d = 12°$, Fig. A2 plots a contour map on the stellar disc of the line-of-sight velocity gradient $\mathrm{d}v_s/\mathrm{d}s \equiv (\hat{s}\cdot\nabla)(\boldsymbol{v}\cdot\hat{s})$ for directional unit vectors $\hat{s}$ from the stellar surface to the position $\{r_p, \theta_p\}$. The heavy black contour for $\mathrm{d}v_s/\mathrm{d}s = 0$ encircles the (blue-shaded) northern region with negative gradient, $\mathrm{d}v_s/\mathrm{d}s < 0$, since these rays cross from the fast wind

[10] To centre on the equatorial disc, we here take θ to be the *latitude*, instead of the *co*-latitude used in standard spherical coordinates.

[11] Often dubbed a 'beta velocity law', with here the velocity exponent $\beta = 1$.

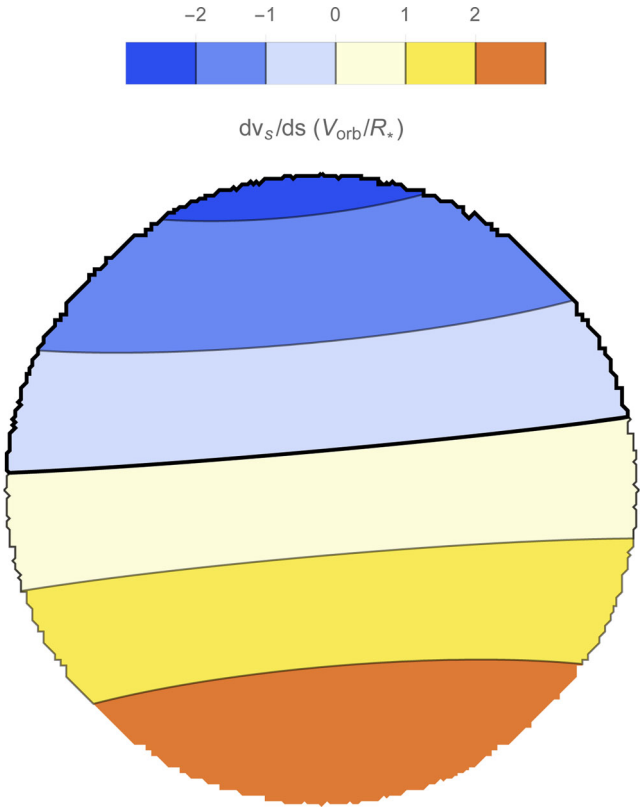

Figure A2. Contour map on the stellar core of projected velocity gradient $\mathrm{d}v_s/\mathrm{d}s$ (in units of $V_{\infty,o}/r_*$) along lines of sight $\hat{s}$ from the star to a radius $r_p = 2\,r_*$ and latitude $\theta_p = 10°$, a position in the middle of the wind–disc boundary layer.

at high-latitude to the slower disc-boundary layer. This is opposite to the strictly positive gradients found in a spherically symmetric, expanding stellar wind, and the associated non-monotonic velocity raises the possibility of multiple line resonances along these rays. The shadowing of the stellar radiation by an inner resonance can reduce the line-driving in the disc and/or its surface layers. For optically thick lines, the shadowed intensity illuminating the wind–disc point is set by the source function at the line resonance, $I_o(r_p, \theta_p) = S(\boldsymbol{r}_{\rm res})$.

To quantify this effect, we next use standard root finding methods to locate such inner resonances $\boldsymbol{r}_{\rm res}$. In principle, determining the resonant source function $S(\boldsymbol{r}_{\rm res})$ requires a self-consistent treatment of all the non-local couplings among global multiple resonances. Instead, we choose here to simply characterize this in terms of an *optically thin* source function that merely accounts for the geometrical dilution of the mean intensity from the stellar core, giving then

$$I_o(r_p,\theta_p) \approx S_{\rm thin}(r_{\rm res}) \equiv I_{\rm core}\left[1 - \sqrt{1 - (r_*/r_{\rm res})^2}\right]. \tag{A4}$$

Unshadowed rays without any such inner resonance still have $I_o = I_{\rm core}$; ignoring any limb darkening, we take this to be constant over the stellar disc.

For this same wind–disc boundary point ($r_p = 2\,r_*$, $\theta_p = 12°$) taken for Fig. A2, the central panel of Fig. A3 maps contours of the illuminating intensity I_o from the associated directions towards the stellar disc. All the Northern hemisphere regions with a negative line-of-sight gradient in Fig. A2 have reduced intensity, due to the shadowing by the inner resonance. But note that there is also a sliver along the left limb in the south where the intensity is

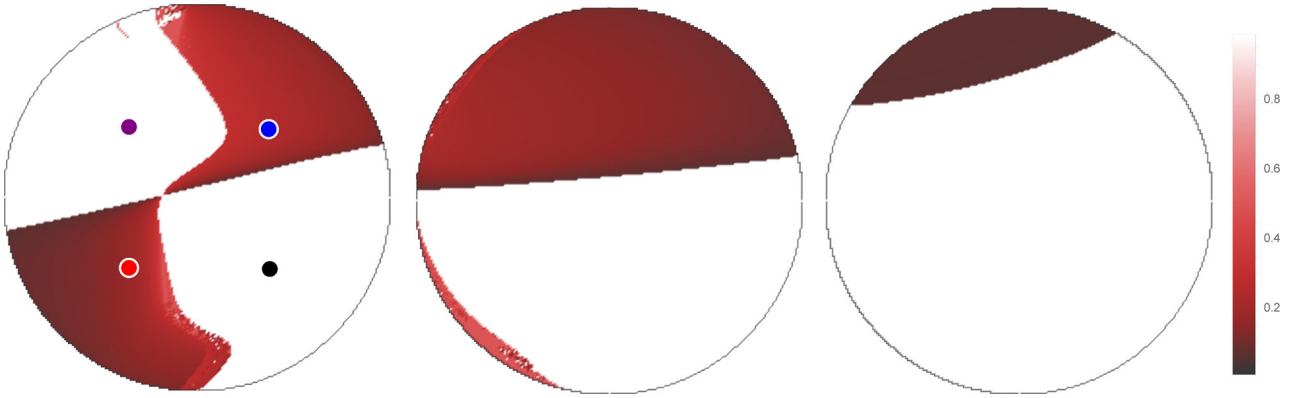

Figure A3. Colour maps on the stellar core of intensity I_o (in units of core intensity I_{core}) illuminating the positions at radius $r_p = 2\,r_*$, with the left-hand, centre, and right-hand panels showing results for position latitudes $\theta_p = 8°$, 10°, and 12° that are below, within, and above the wind–disc boundary layer. The four coloured dots in the leftmost panel represent sight lines for the projected velocity plots in Fig. A4.

also reduced, indicating that even these directions with a positive velocity gradient at the specified wind–disc point have an interior resonance that reduces the intensity.

None the less, over more half the stellar disc, mostly in the Southern hemisphere that illuminates the point from below, through the disc, there is no inner resonance. The unattenuated illumination from these regions thus can sustain the line-driving, albeit with a reduction in strength. In this example, this amounts to a flux reduction factor of 0.65 if one assumes the thin source function at the resonance, or a factor of 0.54 if one assumes complete absorption at this resonance.

As shown in the right-hand panel of Fig. A2, at the higher latitude $\theta_p = 16°$ above the disc–wind boundary, the covering fraction in the Northern hemisphere shrinks, weakening the line driving reduction. Indeed, for $|\theta_p| > 18°$, one recovers full illumination without any attenuation.

At lower latitudes within the wind–disc boundary, the Keplerian shear of the disc plays an important role in the formation or inhibition of an inner resonance. The left-hand panel of Fig. A3 shows that for latitude $\theta_p = 8°$ this leads to an increase in the shadowing arc on the left-hand side of the Southern hemisphere, but with a corresponding *decrease* in the resonance covering in the left-hand side of the Northern hemisphere.

For this disc viewpoint, Fig. A4 plots the spatial variation of light-of-sight velocity for sight lines towards the four quadrants of the stellar disc. This illustrates how the sight lines towards the upper right (blue) and lower left (red) quadrants have an inner resonance (connected by dashed lines), while the two other sight lines have no such resonance, even though the velocity along the sight to the upper right quadrant is non-monotonic, with a negative local velocity gradient at the considered viewpoint.

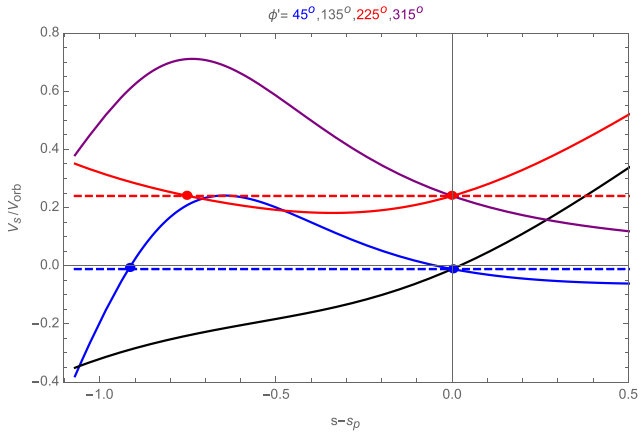

Figure A4. For that same disc viewpoint ($r_p = 2\,r_*$; $\theta_p = 8°$) used for the leftmost panel of Fig. A3, line plots of the spatial variation of velocity component v_s along the four sight lines towards the stellar core shown by the coloured dots in that figure. These all have impact parameter $p = 0.5\,r_*$ from stellar disc centre, but with distinct orientations set by polar angles $\phi' = 45°$, 135°, 225°, and 315° (solid lines colored blue, black, red, and purple), representing stellar quadrants ranging clockwise from upper right to upper left. The red and blue dashed curves connect the local velocity at the viewpoint to a common projected velocity at an inner resonance closer to the star, as signified by the red and blue dots. The black and purple curves have no such inner resonance.

A3 Flux reduction

Finally, by integrating the illumination intensity I_o over the area of the stellar disc for any range of wind/disc viewpoints, we can compute the spatial dependence of the associated flux reduction factor. This then provides an estimate of the associated reduction of the local radiative driving relative to a computation that, as in our simulation models, neglects the effect of multiple line resonances.

Fig. A5 shows a colour map of this flux reduction factor, plotted as a function of wind/disc point radius (on a log scale) and latitude. Note that the strongest reduction, with a value just below 0.6, occurs

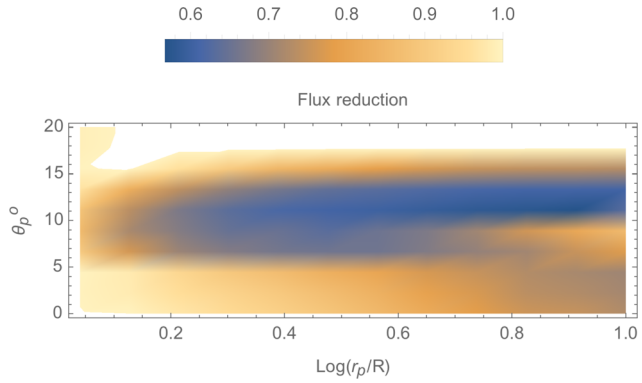

Figure A5. Colour map of the flux reduction from inner resonance shadowing, plotted versus log radius $\log(r_p/r_*)$ over latitudes from the equator to a maximum $\theta_p = 20° > \theta_d$ above the wind–disc boundary.

along a band centred on the wind–disc boundary latitude $\theta_d = 12^\circ$. The reduction weakens near the stellar surface, and towards the equator, and approaches unit value at high latitudes $\theta_p > 18^\circ$ above the wind–disc boundary.

If one assumes optically thick pure *absorption* at the inner resonance – instead of an optically thin source function for forward-scattered radiation – then the flux reduction is generally about 10 per cent stronger. On the other hand, a solution that self-consistently accounts for the scattered radiation coupling among global resonances could increase this inner resonance source function, with then a weakening of the associated flux reduction in radiative driving.

The overall upshot is then that accounting for multiple resonance in the wind+disc simulations here should result in at most a modest, factor 2 reduction in the line force, with the greatest effect concentrated around wind–disc boundary layer. The reduction should be weaker in the disc mid-plane, and approach unity above the disc in the high-speed wind.

This paper has been typeset from a TEX/LATEX file prepared by the author.